PAPER

Check for updates

NiCoP–CeO$_2$ composites for efficient electrochemical oxygen evolution†

Jiyu Li, Zeyan Wang, [iD] * Peng Wang, [iD] Zhaoke Zheng, [iD] Yuanyuan Liu, [iD] Hefeng Cheng and Baibiao Huang [iD] *

In this study, a novel NiCoP–CeO$_2$ composite was constructed on a Ni foam by a simple hydrothermal method and thermal phosphating strategy. In the OER test, NiCoP–CeO$_2$ exhibited a low overpotential of 217 mV at 10 mA cm^{-2}, 45 mV dec^{-1} of Tafel slopes. With the help of theoretical calculations and experimental characterization, the reason for performance improvement was analyzed in depth. The results show that CeO$_2$ leads to a confinement effect, maintaining the nanosheet morphology of NiCo-LDHs, which contributes to sustaining the catalyst in favourable contact with H$_2$O and minimizing the OER potential. Furthermore, by loading CeO$_2$ onto NiCoP, the hydrophilicity of the catalyst is significantly enhanced. Our work provides an ingenious synthesis strategy for the preparation of efficient and inexpensive electrocatalytic materials.

1. Introduction

Hydrogen is one of the most promising alternatives to traditional fossil fuels because it is considered a green fuel with very high energy density.[1] Among the strategies for hydrogen production, electrochemical water splitting is regarded as one of the most promising methods due to its availability and operability.[2] However, the slow kinetics of anodic oxygen evolution (OER) reactions seriously affect the splitting efficiency of water.[3] So far, noble metal oxides, such as ruthenium (Ru) and iridium (Ir) based oxides, are widely used as the reference catalysts for OER processes. However, due to the scarcity of natural resources and high cost, its large-scale application is seriously hindered.[4]

Recently, the exploration of noble-metal free OER catalysts, such as LDHs, has attracted increasing interest.[5–9] Among these, earth-abundant 3d transition metal layered double hydroxides (LDHs) in OER have been studied a lot in recent years owing to their excellent catalytic performances and low prices.[10] NiCo-LDHs have attracted considerable attention owing to their abundant active sites and rapid anion exchange, which exhibit excellent OER reactivity close to the noble metal catalysts. Nevertheless, the poor conductivity of LDHs has greatly restricted their OER performance. Hence, to improve the conductivity of LDHs, some methods have been recently developed in recent years, such as sulfuration, phosphating, and selenizing. Among them, transition metal phosphides

(TMPs) obtained by phosphating have been widely studied. NiCoP is converted from NiCo-LDHs by phosphating, which can significantly improve the electrical conductivity. Besides, transition metal phosphates exhibit superior catalytic activity due to their catalytic mechanism being similar to the hydrogenase.[10,11] However, although its conductivity and catalytic activity are improved, the morphology and chemical properties of the catalyst are easily damaged in the phosphating process and hydrophilicity of the catalyst is severely weakened.[12] Moreover, catalysts are mostly oxidized in the OER process because of the high catalytic activity of NiCoP, and it results in poor stability during the long-term OER process.

Compared to phosphates, oxides tend to perform better in stability and hydrophilicity. Consequently, combining oxides with NiCoP may yield a composite with excellent catalytic activity, NiCoP's conductivity and stability, and oxides' hydrophilicity, which has proven to be an effective method in the fields of catalysis.[13–17] CeO$_2$, as a widely used oxide, exhibits some attractive attributes, such as great stability, hydrophilicity, high oxygen storage capacities, reversible surface oxygen ion exchange and good electronic/ionic conductivity.[18] Moreover, CeO$_2$ contains the oxidation states of Ce^{3+} and Ce^{4+}, which results in the presence of oxygen vacancies to maintain the charge neutrality. Oxygen vacancy on the surface of CeO$_2$ can not only serve as an oxygen buffer for efficient oxygen supply but also enhance its hydrophilicity, which is important for electrocatalytic OER.[19] Owing to the above-mentioned properties of CeO$_2$, if we load CeO$_2$ on the surface of NiCoP to construct a NiCoP–CeO$_2$ composite, it is expected to maintain the original properties of both CeO$_2$ and NiCoP, which could further improve the OER performances and stability of NiCoP.

State Key Laboratory of Crystal Materials, Shandong University, Jinan 250100, China. E-mail: wangzeyan@sdu.edu.cn; bbhuang@sdu.edu.cn

In this study, we report a novel NiCoP–CeO$_2$ composite electrocatalyst synthesized by a simple hydrothermal method and thermal phosphating strategy. The presence of CeO$_2$ in the composites can not only perfectly preserve the nanosheet morphology but can also improve the hydrophilicity of the material in a synergistic way. Furthermore, theoretical calculations show that the H$_2$O adsorption energies of NiCoP can be greatly lowered with the assistance of CeO$_2$. The optimized NiCoP–CeO$_2$ catalyst exhibits an overpotential of 217 mV at 10 mA cm^{-2} and Tafel slope of 45 mV dec^{-1}. Surprisingly, the stability of the NiCoP–CeO$_2$ composites was also greatly improved, and no obvious decline on current density was observed after 10 h in the alkaline electrolyte solution (KOH, pH = 13.8). Moreover, after the stability test, the XPS results changed slightly compared to before. The structure characterization and electrochemical test results show that the introduction of CeO$_2$ to the catalyst provides a feasible strategy to improve the OER performance of TMP electrocatalysts.

2. Experimental section

2.1 Materials

Ni foam (99.9%, HF-Kejing), nickel nitrate hexahydrate (Ni(NO$_3$)$_2$·6H$_2$O, 99%, Sinopharm Chemical Reagent Co. Ltd), cobalt nitrate hexahydrate (Co(NO$_3$)$_2$·6H$_2$O, 99%, Sinopharm Chemical Reagent Co. Ltd), cerium nitrate hexahydrate (Ce(NO$_3$)$_3$·6H$_2$O, 99%, Sinopharm Chemical Reagent Co. Ltd), urea (CH$_4$N$_2$O, 99%, Sinopharm Chemical Reagent Co. Ltd), sodium hypophosphite monohydrate (NaH$_2$PO$_2$·H$_2$O, 99%, Aladdin), cetyltrimethylammonium bromide (C$_{19}$H$_{42}$BrN, 99%, Aladdin), methanol (CH$_3$OH, 99%, Sinopharm Chemical Reagent Co. Ltd) and ultrapure water (18.2 MΩ cm) were used without any further treatment.

2.2 Synthesis of the NiCo-LDHs

A Ni foam was washed ultrasonically in 1 M hydrochloric acid, acetone and ethanol for 30 min respectively to remove the surface oxide layer and organic species. Then, 0.63 mmol nickel nitrate hexahydrate (Ni(NO$_3$)$_2$·6H$_2$O), 0.07 mmol cobalt nitrate hexahydrate (Co(NO$_3$)$_2$·6H$_2$O) and 0.25 g CTAB (C$_{19}$H$_{42}$BrN) were added in a mixed solution of 3 ml ultrapure water and 15 ml methanol (CH$_3$OH) under stirring to form a clear solution with vigorous stirring for about 20 min. After stirring, the solution was poured in a Teflon autoclave and a piece of Ni foam was immersed in it. Then, the Teflon autoclave was heated in an oven at 180 °C for 12 h. After cooling down to 25 °C, the Ni foam was washed by deionized water and ethanol four times. After drying, this obtained sample was named NiCo-LDHs.

2.3 Synthesis of the NiCoP–CeO$_2$ precursors

0.6 mmol cerium nitrate hexahydrate (Ce(NO$_3$)$_2$·6H$_2$O) and 1 mmol urea were added in a 15 ml distilled water under stirring to form a clear solution with vigorous stirring for about 20 min. After stirring, the solution was poured in a Teflon autoclave and a piece of the NiCo-LDH electrode was immersed in it. Then, the Teflon autoclave was heated in an oven at 180 °C for 12 h. After

cooling down to 25 °C, the Ni foam was washed by deionized water and ethanol four times. After drying, this obtained sample was named NiCoP–CeO$_2$ precursors. It should be noted that different precursors can be synthesized with different molarities of cerium nitrate hexahydrate.

2.4 Synthesis of the NiCoP–CeO$_2$

0.5 g of hypophosphite monohydrate (NaH$_2$PO$_2$·H$_2$O) and a piece of NiCoP–CeO$_2$ precursor were put in a porcelain boat with NaH$_2$PO$_2$·H$_2$O placed in the upper tuyere. They were heated at 300 °C for 2 h under Ar atmosphere in a tube furnace. After the reaction, the sample was taken and named NiCoP–CeO$_2$.

2.5 Characterizations

An X-ray diffractometer (XRD, Bruker AXS D8 diffractometer) was used for obtaining the structural information of the samples. For ascertaining the valence state and chemical composition, the samples were studied using X-ray photoelectron spectroscopy (XPS, Thermo Fisher Scientific Escalab 250 spectrometer). The microstructures of the samples were further detected by scanning electron microscopy (SEM, Hitachi S-4800) and high-resolution transmission electron microscopy (TEM, Talos F200X). The weight change of the wet samples was obtained by thermogravimetric analysis (TG, Mettler-Toledo TGA/DSC/1600HT). To determine the chemical desorption temperature, the sample was studied by temperature programmed desorption (TPD, Micromeritics AutoChem II 2920).

2.6 Computational methods

All calculations were based on the density functional theory (DFT) and performed with the Vienna *Ab initio* Simulation Package (VASP) code.[20,21] The exchange and correlation energy functional was expressed in the GGA-PBE.[22] The projector-augmented wave method[23,24] was used to describe the interactions between ions and electrons. The valence electrons were solved in the plane-wave basis with a cut-off energy of 400 eV. The convergence criteria for the energy calculation and structure optimization were set to 1.0×10^{-5} eV and a force tolerance of 0.05 eV Å^{-1}, respectively. The Brillouin-zone integration was performed using a $1 \times 1 \times 1$ $\varGamma$-centered k-point mesh with a Gaussian smearing set to 0.05 eV. To accurately describe the localization of Ce 4f electrons, we conducted the DFT + U calculations with a value of $U_{\text{eff}} = 5$ eV. The adsorption energy was defined by

$$E_{\text{ads}} = E(\text{adsorbate/surface}) - E(\text{adsorbate}) - E(\text{surface})$$

where $E(\text{adsorbate/surface})$ is the total energy of a surface interacting with adsorbate, and $E(\text{adsorbate})$ and $E(\text{surface})$ are the energies of the isolated adsorbate and clean surface, respectively.

2.7 Electrochemical measurements

The OER performance of the material was measured in an alkaline environment using a standard three-electrode system.

A Hg/HgO electrode was used as the reference electrode, a graphite rod electrode was used as the counter electrode, and a phosphide electrode was used as the working electrode. All the experiments were carried out in a 1.0 M KOH (pH = 13.8) solution using the CHI660E electrochemical workstation. The surface area, overpotential, stability and resistance of the electrode were measured by cyclic voltammetry (CV), linear sweep voltammetry (LSV), chronoamperometry curve (i–t) and electrochemical impedance spectroscopy (EIS). In particular, CV was performed at a scan rate of 100 mV s^{-1} for different cycles, until steady CV curves were obtained in 1 M KOH solution: the scanning rate of LSV test was 2 mV s^{-1}; the percentage of iR correction is 90%; the stability test time was 10 hours; the EIS test amplitude was 5 mV, the frequency range was between 10^{-2} and 10^5 Hz, and the applied potential was 1.58 V ($vs.$ RHE). The conversion formula was $\Delta E_{(\text{RHE})} = E + 0.059 \times \text{pH} + 0.098$.

3.   Results and discussion

The NiCoP–CeO$_2$ working electrode was prepared following the procedure, as illustrated in Fig. 1. First, NiCo-LDHs were prepared by the hydrothermal method. Then, the Ni foam coated with NiCo-LDHs reacted again to load the Ce compound, which may be cerium oxide carbonate hydrate (Fig. S1†). Finally, the NiCoP–CeO$_2$ precursor was placed in a tube furnace and heated at 573 K under Ar atmosphere for 2 h. The final product was NiCoP–CeO$_2$. Simultaneously, by adjusting the load of CeO$_2$, the best ratio of NiCoP and CeO$_2$ was obtained, which was named NiCoP–CeO$_2$. Samples with amount of 0.72 and 0.48 mmol Ce(NO$_3$)$_2$·6H$_2$O in the preparation process were named NiCoP–CeO$_2$M and NiCoP–CeO$_2$L (Fig. S2†), respectively. For comparison, NiCoP was synthesized by the same method without cerium sources. The crystal structure and composition of NiCoP–CeO$_2$ were investigated by an X-ray diffractometer (XRD). As for NiCoP–CeO$_2$, the characteristic peaks match well with different standard cards, including JCPDS no. 89-8436 (CeO$_2$), JCPDS no. 71-2336 (NiCoP) and JCPDS no. 70-0989 (Ni foam), which indicated that CeO$_2$ and NiCoP are successfully synthesized on the Ni foam (Fig. 2a). The peak of CeO$_2$ and NiCoP is not obvious, which may be attributed to the strong peak of Ni foam.
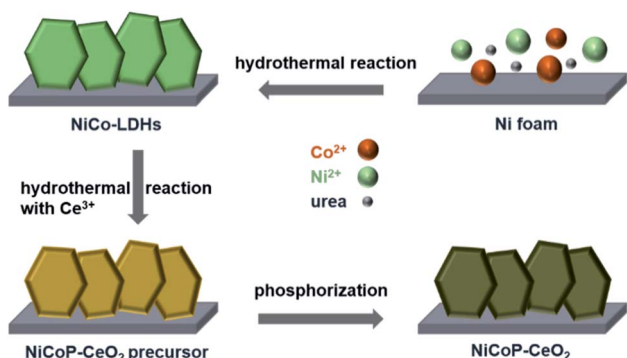

Fig. 1 The synthetic scheme of the NiCoP–CeO$_2$ electrode.
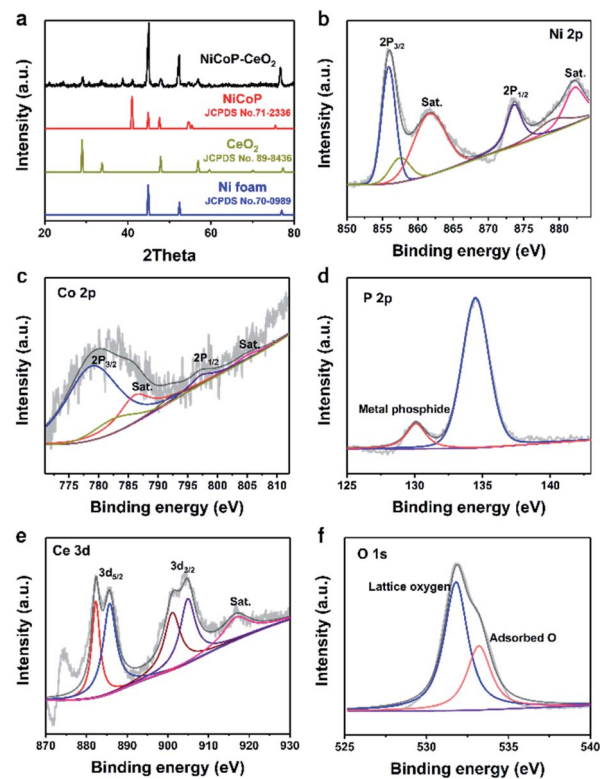

Fig. 2 XRD patterns of NiCoP–CeO$_2$ (a); Ni 2p (b), Co 2p (c), P 2p (d), Ce 3d (e), O 1s (f) XPS spectra of NiCoP–CeO$_2$.

To further investigate the chemical composition and valence of the samples, X-ray photoelectron spectroscopy (XPS) was used. The full spectrum of NiCoP–CeO$_2$ (the sample with the best performance, Fig. S3†) demonstrates the presence of Ni, Co, P, Ce and O elements, and the peak positions of all the elements are corrected according to the normative C 1s peak (284.8 eV). As shown in Fig. 2b, Ni 2p spectra could be fitted into
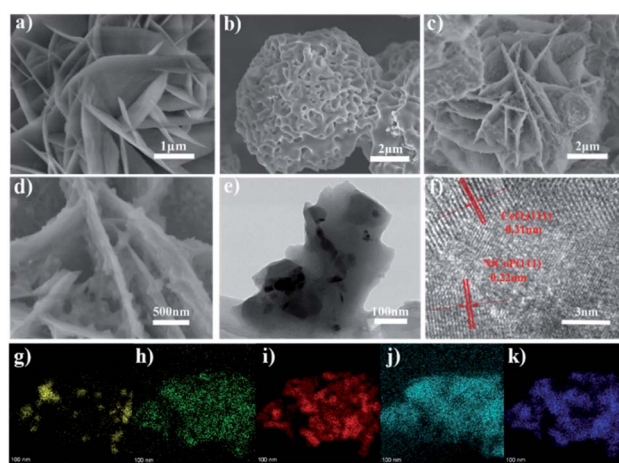

Fig. 3 SEM images of NiCo-LDHs (a), NiCoP (b), low (c) and high (d) magnification of NiCoP–CeO$_2$; TEM (e) and HRTEM (f) images of NiCoP–CeO$_2$; EDX mapping images and elements of Ce, Co, Ni, O and P elements in NiCoP–CeO$_2$ (g–k).

two doublet peaks at 874.1 eV and 856.2 eV with two satellites, respectively, which can be ascribed to Ni^{2+}, Ni^{3+}, $Ni–PO_x$ and Ni–P, indicating the formation of nickel phosphide.[25,26] The Co 2p (Fig. 2c) spectra of the NiCoP samples are divided into two spin–orbit doublets at 778.9 eV and 797.4 eV as well as two satellites at 787.1 eV and 805.1 eV, formed due to the presence of Co^{2+}.[27,28] The P 2p spectra (Fig. 2d) exhibits a peak at 134.2 eV, which can be assigned to the P in the phosphide. In addition, the peak at 130.1 eV tends to represent metal phosphide.[29] The Ce 3d XPS spectrum (Fig. 2e) displays six main peaks at 882.1, 900.9 and 916.5 eV, which can be ascribed to the Ce^{4+} state. The peaks at 885.1 eV and at 905.2 eV can be attributed to the Ce^{3+} state, which illustrate the coexistence of Ce^{4+} and Ce^{3+} species on the surface of the $NiCoP–CeO_2$ sample.[30,31] Moreover, the XPS spectrum of O 1s in Fig. 2f displays two peaks at 531.9 eV and 533.4 eV, representing the lattice oxygen and adsorptive oxygen species, respectively.[32] Besides, the presence of Ce^{3+} and adsorptive oxygen species indicates abundant oxygen vacancies in the sample, which plays a great role in enhancing the adsorption of H_2O, increasing the electrical conductivity, reducing the activation energy of OER and consequently promoting the electrochemical catalysis performance.[33]

To further study the morphology and microstructure of samples, scanning electron microscopy (SEM) and transmission electron microscopy (TEM) were also carried out. As shown in Fig. S4† and 3c, NiCo-LDHs, $NiCoP–CeO_2$ precursors and $NiCoP–CeO_2$ all show nanosheet structure. NiCo-LDHs exhibit nanosheet morphology with a smooth surface (Fig. 3a). After loading with the Ce compound on $NiCoP–CeO_2$ precursors, the nanosheets became thicker and some attachments appeared on the surface of the sample (Fig. S4b†). After being heated at a high temperature, the Ce compound loaded on the surface was transformed into CeO_2 and was uniformly coated on the surface of the nanosheets (Fig. 3c). Moreover, NiCo-LDHs effectively phosphated and transformed into NiCoP (Fig. 3b and S5†). As for $NiCoP–CeO_2$, different from the NiCoP sample, although the phosphating process occurs during the heat treatment of NiCo-LDHs, the generated CeO_2 displays a confinement effect, which can inhibit the agglomeration of NiCoP and maintain the stability of the structure. Therefore, the obtained $NiCoP–CeO_2$ still maintains the nanosheet structure of $NiCoP–CeO_2$ on the micro level. As shown in the high magnification picture (Fig. 3d), the surface of the nanosheets is uneven and contains numerous particles, which indicates that NiCoP and CeO_2 are effectively bound together. The high-resolution transmission electron microscopy image (HRTEM, Fig. 3f) shows that the (111) facet of NiCoP and the (111) facet of CeO_2 appears in $NiCoP–CeO_2$, proving the successful formation of the composite interface, which is conductive to the charge transfer between NiCoP and CeO_2.[34,35] Besides, the energy dispersive X-ray elemental mapping spectroscopy (EDX mapping) indicates that the Ni, Co, P, Ce, O elements are uniformly distributed on the $NiCoP–CeO_2$ composite (Fig. 3g–k).

To further research the electrocatalytic OER performance of different materials, a series of electrochemical experiments were carried out in a three-electrode system with 1 M KOH solution. There are several linear sweep voltammetry (LSV) curves of all
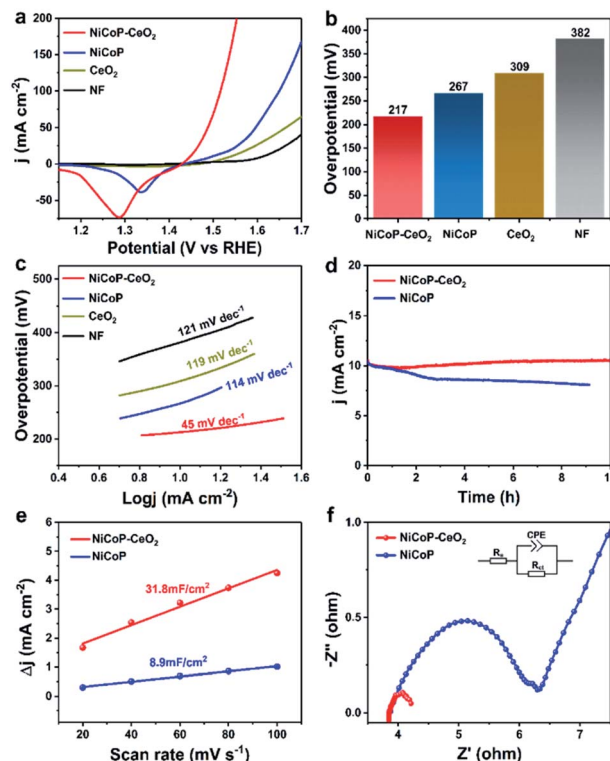

Fig. 4 LSV curves of Ni foam, NiCoP, CeO_2 and $NiCoP–CeO_2$ electrodes in 1 M KOH solution (a); the overpotential of different electrodes at 10 mA cm^{-2} (b); Tafel slope of Ni foam, NiCoP, CeO_2 and $NiCoP–CeO_2$ electrodes (c); the stability test of $NiCoP–CeO_2$ and NiCoP electrode (d); electrochemical surface area of NiCoP and $NiCoP–CeO_2$ electrodes calculated by double layer capacitance (e); electrochemical impedance spectroscopy (EIS) curves of NiCoP and $NiCoP–CeO_2$ electrodes (f).

samples in Fig. 4a. The overpotential of Ni foam, CeO_2, NiCoP, and $NiCoP–CeO_2$ are 382, 309, 267 and 217 mV at 10 mA cm^{-2}, respectively, as shown in Fig. 4b. It can be seen from the figure mentioned above that the overpotential of the material was significantly reduced by loading CeO_2, which proves that the electrocatalytic performance of the material is significantly enhanced by the combination of CeO_2. In order to explore the kinetics of OER, the Tafel slopes of different electrodes were calculated according to the formula: $\eta = b \times \log|j| + a$ (Fig. 4c, including a: corresponding constant; b: Tafel slope; η: overpotential).[36,37] The values of each electrode are as follows: Ni foam (121 mV dec^{-1}), CeO_2 (119 mV dec^{-1}), NiCoP (114 mV dec^{-1}) and $NiCoP–CeO_2$ (45 mV dec^{-1}). As expected, the $NiCoP–CeO_2$ electrode exhibits a much lower Tafel slope compared to NiCoP or CeO_2 electrode, indicating the strong interaction between NiCoP and CeO_2. Besides, Table S1† shows the OER activity of other $LDHs-CeO_2$ composite electrocatalysts. It can be seen that $NiCoP–CeO_2$ exhibits excellent OER performance compared with other materials. In addition, the stability is also a very crucial parameter, as shown in Fig. 4d. After 10 h of the reaction, the performance of $NiCoP–CeO_2$ visually remained unchanged compared with that of NiCoP. This may be due to the confinement effect of loading CeO_2, which can help the material

to maintain the sheet shape and good contact with H_2O. To further investigate the stability of the material in depth, the $NiCoP–CeO_2$ electrode after the stability test is also characterized (Fig. S6a–f†). The XPS results show that the peak of metal phosphide is slightly weakened (Fig. S6d†), which may be caused by anodic oxidation. However, the amount of Ce^{3+} and adsorbed oxygen is basically unchanged (Fig. S6e and f†). It indicates that the material still contains abundant oxygen vacancies, which proves that $NiCoP–CeO_2$ exhibits good stability. Moreover, electrochemical surface area (ECSA) tests were also performed to measure the amount of the active sites on the materials. Since the value of electric double layer capacitance (EDLC) is proportional to ECSA, the value of EDLC is used to represent the ECSA.[38] As shown in Fig. 4e, the ECSA of $NiCoP–CeO_2$ (31.8 mF cm^{-2}) is nearly triple–quintuple higher than that of pure NiCoP (8.9 mF cm^{-2}), which manifests that the confinement effect caused by the introduction of CeO_2 leads to maintaining the nanosheet morphology and therefore expose more active sites in the $NiCoP–CeO_2$ composite. Fig. 4f shows the EIS Nyquist plots of different electrodes and the relevant equivalent circuit diagram simulated by the Z-view software, which contains solution resistance (R_s), charge transfer resistance (R_{ct}) and constant phase element (CPE).[39,40] As shown in the picture, the $NiCoP–CeO_2$ electrode shows lower R_{ct} compared to NiCoP. It confirms that the introduction of CeO_2 greatly improves the charge transfer rate during the OER process.
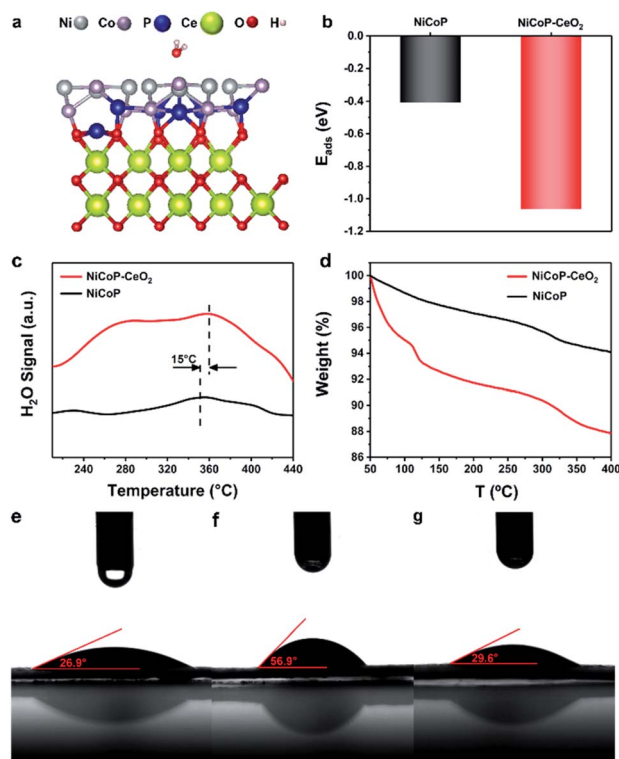
The adsorption structures and original structures on $NiCoP–CeO_2$ and NiCoP are shown in Fig. 5a, S7 and S8,† respectively (Cartesian coordinates in Tables S2 and S3†). It can be seen that their corresponding H_2O adsorption energies (E_{ads}) are shown in Fig. 5b. It appears that $NiCoP–CeO_2$ possesses much lower E_{ads} (−1.06 eV) than that of NiCoP (−0.41 eV), which reveals that coupling CeO_2 with NiCoP enhances the NiCoP's adsorption ability to H_2O for. In the TPD spectra (Fig. 5c), $NiCoP–CeO_2$ shows the larger H_2O adsorption area and the higher desorption temperature, which is consistent with previous theoretical calculation results. Moreover, we carried out TGA tests on wet NiCoP and $NiCoP–CeO_2$ (Fig. 5d), and the results are within our expectations that more weight is lost in $NiCoP–CeO_2$ compared with NiCoP. It means that $NiCoP–CeO_2$ tends to have stronger attraction to H_2O. Subsequently, the difference in the results of the wetting-ability test shown in Fig. 5e–g indicates that phosphating NiCo-LDHs to NiCoP weakens the hydrophilicity of the catalyst. However, $NiCoP–CeO_2$ has a better wetting-ability, even better than that of CeO_2 (Fig. S9†), which indicates that CeO_2 and NiCoP synergically enhanced the hydrophilicity of the material after composite and ultimately leads to the improvement of $NiCoP–CeO_2$'s electrocatalytic performance.

4. Conclusions

In conclusion, the $NiCoP–CeO_2$ electrode was prepared on a Ni foam by a simple hydrothermal method and thermal phosphating strategy. Compared with pure NiCoP, $NiCoP–CeO_2$ displays superior catalytic activity including higher ECSA values, lower overpotential, accelerated kinetic rate. The presence of CeO_2 in the composites not only perfectly preserve the nanosheet morphology but can also improve their hydrophilicity in a synergistic way and stability of the catalyst on the basis of experimental results. Furthermore, theoretical calculations show that the H_2O adsorption energies of NiCoP can be greatly lowered with the assistance of CeO_2. This work provides an ingenious material design method and guidance for the preparation and design of efficient catalysts in the future.

Author contributions

Conceptualization, J. L.; investigation, Z. W.; H. C. and Z. Z.; data curation, Z. W.; formal analysis, J. L.; Z. W. and P. W.; methodology, J. L.; project administration, Z. Z.; Y. L. and B. H.; resources, Y. L.; Z. W. and B. H.; supervision, B. H.; validation, P. W.; Y. L. and B. H.; writing—original draft, J. L.; writing—review & editing, Z. W. and H. C.

Conflicts of interest

There are no conflicts to declare.

Fig. 5 Optimized adsorption structures of $NiCoP–CeO_2$ (a); adsorption energies of H_2O on NiCoP and $NiCoP–CeO_2$ (b); H_2O TPD spectra of NiCoP and $NiCoP–CeO_2$ (c); thermogravimetric analysis of NiCoP and $NiCoP–CeO_2$ (d); wetting-ability testing of (e) NiCo-LDHs, (f) NiCoP and (g) $NiCoP–CeO_2$.

References

1 N. S. Lewis and D. G. Nocera, *PNAS*, 2006, **103**, 15729–15735.

2 B. Xiong, L. Chen and J. Shi, *ACS Catal.*, 2018, **8**, 3688–3707.

3 Z. P. Wu, X. F. Lu, S. Q. Zang and X. W. Lou, *Adv. Funct. Mater.*, 2020, **30**, 1910274.

4 W. Li, J. Liu, P. Guo, H. Li, B. Fei, Y. Guo, H. Pan, D. Sun, F. Fang and R. Wu, *Adv. Energy Mater.*, 2021, **11**, 2102134.

5 T. V. Vineesh, M. P. Kumar, C. Takahashi, G. Kalita, S. Alwarappan, D. K. Pattanayak and T. N. Narayanan, *Adv. Energy Mater.*, 2015, **5**, 1500658.

6 C. Li, L. Xie, J. Zhao, L. Gu, J. Wu and G. Li, *Appl. Catal., B*, 2022, **306**, 121097.

7 B. Liu, M. Zhang, Y. Wang, Z. Chen and K. Yan, *J. Alloys Compd.*, 2021, **852**, 156949.

8 J. Joy, A. Sekar, S. Vijayaraghavan, T. P. Kumar, V. K. Pillai and S. Alwarappan, *J. Electrochem. Soc.*, 2018, **165**, H141–H146.

9 Q. Tu, W. Liu, M. Jiang, W. Wang, Q. Kang, P. Wang, W. Zhou and F. Zhou, *ACS Appl. Energy Mater.*, 2021, **4**(5), 4630–4637.

10 Y. Guo, T. Park, J. W. Yi, J. Henzie, J. Kim, Z. Wang, B. Jiang, Y. Bando, Y. Sugahara, J. Tang and Y. Yamauchi, *Adv. Mater.*, 2019, **31**, 1807134.

11 H. Sun, Z. Yan, F. Liu, W. Xu, F. Cheng and J. Chen, *Adv. Mater.*, 2020, **32**, 1806326.

12 Y. Wang, B. Kong, D. Zhao, H. Wang and C. Selomulya, *Nano Today*, 2017, **15**, 26–55.

13 P. Hao, M. Xie, S. Chen, M. Li, F. Bi, Y. Zhang, M. Lin, X. Guo, W. Ding and X. Guo, *Sci. Adv.*, 2020, **6**, eaay7031.

14 S. Zhang, S. E. Saji, Z. Yin, H. Zhang, Y. Du and C. H. Yan, *Adv. Mater.*, 2021, **33**, 2005988.

15 Y. Zhong, X. Xia, F. Shi, J. Zhan, J. Tu and H. Fan, *Adv. Sci.*, 2016, **3**, 1500286.

16 K. Guo, Y. Wang, S. Yang, J. Huang, Z. Zou, H. Pan, P. S. Shinde, S. Pan, J. Huang and C. Xu, *Sci. Bull.*, 2021, **66**, 52–61.

17 H. Wang, K. H. L. Zhang, J. P. Hofmann, V. A. d. l. P. O'Shea and F. E. Oropeza, *J. Mater. Chem. A*, 2021, **9**, 19465–19488.

18 T. Montini, M. Melchionna, M. Monai and P. Fornasiero, *Chem. Rev.*, 2016, **116**, 5987–6041.

19 X. Wang, Y. Zhang, S. Song, X. Yang, Z. Wang, R. Jin and H. Zhang, *Angew. Chem., Int. Ed.*, 2016, **128**, 4618–4622.

20 G. Kresse and J. Furthmüller, *Phys. Rev. B: Condens. Matter Mater. Phys.*, 1996, **54**, 11169–11186.

21 G. Kresse and J. Furthmüller, *Comput. Mater. Sci.*, 1996, **6**, 15–50.

22 J. P. Perdew, K. Burke and M. Ernzerhof, *Phys. Rev. Lett.*, 1996, **77**, 3865.

23 P. E. Blöchl, *Phys. Rev. B: Condens. Matter Mater. Phys.*, 1994, **50**, 17953–17979.

24 G. Kresse and D. Joubert, *Phys. Rev. B: Condens. Matter Mater. Phys.*, 1999, **59**, 1758–1775.

25 S. Anantharaj, S. Kundu and S. Noda, *Nano Energy*, 2021, **80**, 105514.

26 D. M. Morales, M. A. Kazakova, S. Dieckhöfer, A. G. Selyutin, G. V. Golubtsov, W. Schuhmann and J. Masa, *Adv. Funct. Mater.*, 2019, **30**, 1905992.

27 C. Yang, S. Zai, Y. Zhou, L. Du and Q. Jiang, *Adv. Funct. Mater.*, 2019, **29**, 1901949.

28 X. Yuan, H. Ge, X. Wang, C. Dong, W. Dong, M. S. Riaz, Z. Xu, J. Zhang and F. Huang, *ACS Energy Lett.*, 2017, **2**, 1208–1213.

29 X. Li, A. M. Elshahawy, C. Guan and J. Wang, *Small*, 2017, **13**, 1701530.

30 X. Li, S. You, J. Du, Y. Dai, H. Chen, Z. Cai, N. Ren and J. Zou, *J. Mater. Chem. A*, 2019, **7**, 25853–25864.

31 H. Sun, C. Tian, G. Fan, J. Qi, Z. Liu, Z. Yan, F. Cheng, J. Chen, C. P. Li and M. Du, *Adv. Funct. Mater.*, 2020, **30**, 1910596.

32 D. Chen, D. He, J. Lu, L. Zhou, F. Liu, J. Liu, J. Yu, G. Wan, S. He and Y. Luo, *Appl. Catal., B*, 2017, **218**, 249–259.

33 V. K. Paidi, L. Savereide, D. J. Childers, J. M. Notestein, C. A. Roberts and J. v. Lierop, *ACS Appl. Mater. Interfaces*, 2017, **9**, 30670–30678.

34 C. Du, L. Yang, F. Yang, G. Cheng and W. Luo, *ACS Catal.*, 2017, **7**, 4131–4137.

35 G. Spezzati, A. D. Benavidez, A. T. DeLaRiva, Y. Su, J. P. Hofmann, S. Asahina, E. J. Olivier, J. H. Neethling, J. T. Miller, A. K. Datye and E. J. M. Hensen, *Appl. Catal., B*, 2019, **243**, 36–46.

36 B. Chang, J. Yang, Y. Shao, L. Zhang, W. Fan, B. Huang, Y. Wu and X. Hao, *ChemSusChem*, 2018, **11**, 3198–3207.

37 J. Zhang, C. Zhang, Z. Wang, J. Zhu, Z. Wen, X. Zhao, X. Zhang, J. Xu and Z. Lu, *Small*, 2018, **14**, 1703098.

38 P. Zhou, X. Lv, D. Xing, F. Ma, Y. Liu, Z. Wang, P. Wang, Z. Zheng, Y. Dai and B. Huang, *Appl. Catal., B*, 2020, **263**, 118330.

39 Z. Xue, Y. Li, Y. Zhang, W. Geng, B. Jia, J. Tang, S. Bao, H.-P. Wang, Y. Fan, Z.-w. Wei, Z. Zhang, Z. Ke, G. Li and C.-Y. Su, *Adv. Energy Mater.*, 2018, **8**, 1801564.

40 Z. Chen, Y. Song, J. Cai, X. Zheng, D. Han, Y. Wu, Y. Zang, S. Niu, Y. Liu, J. Zhu, X. Liu and G. Wang, *Angew. Chem., Int. Ed.*, 2018, **57**, 5076–5080.